Neurochemistry International 190 (2025) 106049

Contents lists available at ScienceDirect

Neurochemistry International

journal homepage: www.elsevier.com/locate/neuint

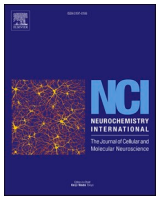

Multi-omics reveals changes in astrocyte fatty acid metabolism during early stages of Alzheimer's disease

Jie Zhong [a], Manhui Li [a], Ziwei Dai [b,*], Jun Wan [a,c,**]

[a] Shenzhen Key Laboratory for Neuronal Structural Biology, Biomedical Research Institute, Shenzhen - Peking University - the Hong Kong University of Science and Technology Medical Center, Shenzhen, Guangdong Province, China
[b] Department of Systems Biology, School of Life Sciences, Southern University of Science and Technology, Shenzhen, Guangdong Province, China
[c] Department of Neuroscience, School of Life Sciences, Southern University of Science and Technology, Shenzhen, Guangdong Province, China

ARTICLE INFO

Keywords:
Multi-omics
Alzheimer's disease
Astrocytes
Fatty acid metabolism

ABSTRACT

Background: Although astrocytes are known to contribute to Alzheimer's disease (AD) progression, their dynamic molecular alterations remain poorly characterized, particularly in early stages of the disease.
Methods: We performed multi-omics profiling (transcriptomics, proteomics, spatial metabolomics) of astrocytes from APP/PS1 and WT mice to characterize dynamic changes during AD progression. To assess similar changes in early human AD, we analyzed single-nucleus RNA sequencing data from human samples.
Results: Transcriptomic analysis of astrocytes from APP/PS1 and WT mice at five time points (2, 4, 6, 9, and 12 months of age) showed notable gene expression differences at 6 months, with reduced activity in fatty acid metabolism pathways (e.g., PPAR signaling, biosynthesis of unsaturated fatty acids). An astrocyte-specific metabolic model confirmed these disruptions. Proteomic analysis corroborated this by showing decreased activity in pathways like butanoate metabolism and PPAR signaling. Spatial metabolomics of brain slices from APP/PS1 and WT mice highlighted fatty acid enrichment in the hippocampus and cortex, alongside differential metabolites specific to the AD mouse model. Single-cell RNA sequencing analysis of human brain samples further showed fatty acid metabolism abnormalities in astrocytes from early AD cases versus controls, emphasizing its role in AD progression.
Conclusion: Our study identified abnormal fatty acid metabolism as an early feature of astrocytes in AD, suggesting an association between dysregulated fatty acid metabolism and disease progression.

1. Background

Alzheimer's disease (AD) is a progressively insidious neurodegenerative disorder characterized by relentless deterioration in memory and cognitive functions (Mahaman et al., 2022). Currently, therapeutic options for AD are limited. While some treatments, such as cholinesterase inhibitors, offer transient improvement in clinical symptoms, they do not target the underlying disease mechanisms (Pathak and Kabra, 2024) (). A small number of emerging therapies are described as disease-modifying based on their potential to slow disease progression; however, their efficacy remains limited and controversial (Sims et al., 2023; van Dyck et al., 2023). In the pathogenesis of AD, the initial deposition of Aβ plaques is followed by the formation of neurofibrillary tangles, which progressively cause structural changes in brain tissue and neuronal loss, ultimately resulting in impairments in memory and cognitive function (Jack et al., 2010, 2013). Notably, the formation of Aβ plaques begins approximately 10–15 years before the onset of clinical symptoms (Drew, 2018). Therefore, investigating the stage of AD characterized by Aβ deposition before clinical symptoms appear is crucial for understanding disease mechanisms and developing interventions to halt disease progression. Several mouse models have been established to investigate Aβ pathology, among which the APP/PS1 model is widely used. In 2-month-old mice (early adulthood), the APP/PS1 model shows no amyloid plaques. In 6-month-old mice (like

* Corresponding author. Department of Systems Biology, School of Life Science, Southern University of Science and Technology, Shenzhen, Guangdong Province, China.
** Corresponding author. Shenzhen Key Laboratory for Neuronal Structural Biology, Biomedical Research Institute, Shenzhen - Peking University - the Hong Kong University of Science and Technology Medical Center, Shenzhen, Guangdong Province, China.
E-mail addresses: daizw@sustech.edu.cn (Z. Dai), wanj@sustech.edu.cn (J. Wan).

https://doi.org/10.1016/j.neuint.2025.106049
Received 23 May 2025; Received in revised form 14 August 2025; Accepted 29 August 2025
Available online 30 August 2025

early-AD stage), noticeable amyloid plaques accumulate in the hippocampus and cortex, without overt behavioral deficits. In 12-month-old mice (like AD-clinical stage), the model exhibits extensive plaque deposition and cognitive impairments (Janus et al., 2015; Volianskis et al., 2010; Lalonde et al., 2005). Its relatively gradual disease progression compared to more aggressive models such as 5 × FAD makes it particularly suitable for studying early-stage AD mechanisms (Richard et al., 2015; Garcia-Alloza et al., 2006).

Previous research on AD primarily focused on neuronal alterations and their functional implications. However, recent studies have elucidated that the pathogenesis of AD extends beyond neuronal loss, implicating astrocytes and other glial cells as critical contributors to disease progression (Uddin and Lim, 2022). Astrocytes, one of the most abundant and largest cell type within the central nervous system (CNS), play a crucial role in maintaining brain homeostasis (Verkhratsky and Nedergaard, 2018; Baldwin et al., 2024). Throughout AD progression, these cells undergo significant morphological and functional changes in both AD patients and animal models. (Verkhratsky et al., 2010, 2019; Nam et al., 2023; Yeh et al., 2011). Notably, the typical senile plaques of AD are composed of aggregated microglia, reactive astrocytes, Aβ deposition and deformed neurites. Astrocytes exhibit dual roles in managing Aβ, inflammation, and oxidative stress, playing intricate roles in the pathology of AD (Bellaver et al., 2023; Lee et al., 2023; Park et al., 2021; Chun and Lee, 2018). Due to the multifaceted nature of astrocyte functions, single-method analyses cannot fully capture the complexity of their molecular programs. Multi-omics technologies offer the potential to track the dynamic progression of AD from a healthy to a diseased state, providing crucial insights into disease mechanisms and facilitating the identification of effective therapeutic targets. Despite advances in multi-omics studies highlighting astrocyte changes related to lipid metabolism, ion balance, neuronal support, and inflammatory responses in AD (Murdock, 2023; Sekar et al., 2015; Mathys et al., 2019), a comprehensive understanding of the dynamic changes of astrocytes remains unknown. In particular, the roles and metabolic shifts of astrocytes in the early stages of AD are still poorly characterized.

To study the dynamic changes in astrocytes during AD, particularly at early stages, we employed a multi-omics approach, including transcriptomics, proteomics, spatial metabolomics, and single-cell omics. By leveraging data from both AD animal models and human samples, we systematically observed disruptions in fatty acid metabolism within astrocytes during the early phase of AD. These findings contribute to a growing body of evidence implicating astrocytic metabolic alterations in early AD and may help inform future investigations into therapeutic strategies or dietary modulation.

2. Methods

2.1. Mice

APPswe/PS1ΔE9 (APP/PS1) double-transgenic mice were obtained from the Model Animal Research Center of Nanjing University, originally derived from the B6.Cg-Tg (APPswe/PS1ΔE9) 85Dbo/Mmjax line (JAX#034832). All APP/PS1 mice used in this study were hemizygous. Breeding was performed by crossing hemizygous APP/PS1 mice with wild-type (WT) mice. Offspring included both hemizygous APP/PS1 mice and WT littermates, which were used as controls. Mice were housed under SPF conditions with a controlled light-dark cycle. Genotyping was performed at postnatal day 21–28 using PCR from ear biopsy DNA. All procedures were approved by the Animal Use and Care Committee of SPHMC (protocol #2022-014), and efforts were made to minimize animal use and suffering.

2.2. Astrocytes isolation by magnetic activated cell sorting (MACS)

Astrocytes were isolated from WT and AD model mice. Mice were deeply anesthetized with 0.7 % pentobarbital sodium (0.1–0.2 mL/10 g body weight, i.p.), and whole brains were collected and placed in ice-cold calcium- and magnesium-free Hanks' Balanced Salt Solution (HBSS; Thermo Fisher, 14170138). Tissue dissociation was performed using the Adult Brain Dissociation Kit (Miltenyi, 130-107-677) with the gentleMACS™ Octo Dissociator (program 37C_ABDK_01). Astrocytes were magnetically labeled with *anti*-ACSA-2 microbeads (Miltenyi, 130-097-678) and isolated using LS columns on an OctoMACS™ separator according to the manufacturer's instructions.

2.3. Immunostaining and imaging

Brains from male mice ($n = 3$ per group) were fixed, cryoprotected, sectioned (20 μm), and processed for immunostaining. For MALDI-MSI analyzed sections, matrix was removed using ethanol washes, followed by 4 % PFA fixation (Wang et al., 2022). Sections were blocked, incubated with primary antibodies (*anti*-GFAP, 1:400, BOSTER; *anti*-β-Amyloid, 1:200, Biolegend), followed by fluorescent secondary antibodies and DAPI. Imaging was performed with Zeiss Celldiscoverer 7, Olympus VS200, or 3DHISTECH Pannoramic MIDI.

2.4. RNA sequencing (RNA-seq) analysis

The astrocyte RNA-seq dataset (GSE137028) (Pan et al., 2020) was previously generated by our lab in a study focused on aging in WT glial cells, though it also contains AD model data. The dataset comprises male WT and APP/PS1 mice at 2, 4, 6, 9, and 12 months of age ($n = 3$ per group).

For singular value decomposition (SVD) analysis, FPKM values were used to select the top 10,000 genes ranked by MAD. The data were log10-transformed and Z-score normalized across columns, yielding a matrix (Matrix A) of 9528 genes × 30 samples, representing AD and WT groups at 2-, 4-, 6-, 9-, and 12-month time points. SVD was then applied to decompose Matrix A. The SVD theorem (The Singular Value Decomposition (SVD), 2002) states that the matrix A can be written as

$$A = U\Sigma V^T,$$

where U (a 9528 × 9528 matrix) and V (a 30 × 30 matrix) are orthogonal and Σ (a 9528 × 30 matrix) is a diagonal matrix containing the singular values. These r singular values are the square roots of the non-zero positive eigenvalues of both AA^T and A^TA, sorted in descending order of magnitude. The different columns in the ΣV^T matrix correspond to the times at which the corresponding expression data are measured, each row in ΣV^T matrix represents an adjusted feature mode, capturing distinct patterns of gene expression influenced by the magnitude of the corresponding singular values. We termed the first row of ΣV^T as mode 1. The contribution of each gene to mode 1 is calculated by the squared values of the first column of the left singular vector $\left(U_{j,1}\right)^2$.

For the Short Time-series Expression Miner (STEM)(Ernst and Bar-Joseph, 2006), FPKM values were used to select the top 10,000 genes ranked by MAD. $\mathrm{Log_2}$(AD/WT) ratios were calculated for 2-, 4-, 6-, 9- and 12-month time points, with the value at 2 months serving as the reference baseline (set to zero) to evaluate temporal progression. The processed data were analyzed in STEM with the number of model profiles set to 20 and default settings otherwise.

Differentially expressed genes (DEGs) were identified using DESeq2 (Love et al., 2014) with adjusted $p < 0.05$ and $|\log_2 FC| > 0.5$. GO-BP (Thomas et al., 2022) and KEGG (Kanehisa et al., 2023) pathway enrichment analyses were performed using clusterProfiler (Yu et al., 2012), and results were visualized with ggplot2 (Wickham, 2016) or Cytoscape (Shannon et al., 2003). In Cytoscape, enrichmentMap was used to construct a similarity-based GO network (Jaccard + Overlap > 0.375), and clusters were annotated using the Markov Cluster Algorithm. Genes in STEM profile were intersected with DEGs at 6 months using the VennDiagram (Chen and Boutros, 2011) package.

Whole cortex transcriptomes from 6-month-old APP/PS1 and WT

mice were generated in our laboratory and are accessible under GEO accession GSE132177 (Ma et al., 2019). Similarly, microglia transcriptomes from 6-month-old APP/PS1 and WT mice were also generated in our laboratory and are available under GEO accession GSE137028 (Pan et al., 2020).

2.5. Quantitative RT-PCR validation of selected genes

Total RNA was extracted from astrocytes isolated from 6-month-old male APP/PS1 and WT mice ($n = 3$ per group) using an RNA-easy Kit (Vazyme). cDNA was synthesized using a reverse transcription kit (Promega). Quantitative PCR was conducted with SYBR Green (Roche) on a Roche LC480 system under standard cycling conditions. Gene expression was quantified relative to Gapdh using the $2^{-\Delta\Delta Ct}$ method. Primer sequences are provided in Additional file: Table S3.

2.6. Generation of astrocyte-specific genome-scale metabolic model (GEM)

The astrocyte-specific GEM was constructed using the getINITModel2 (Agren et al., 2014) function that implements the tINIT algorithm for reconstruction of cell-type-specific GEMs, with essential metabolic tasks provided in Dataset S1. Input data consisted of the average TPM values of genes expressed in WT astrocytes across all ages. Genes with TPM values of 1 or higher were considered as actively expressed, while genes with TPM values below this threshold were deemed lowly expressed. The Mouse1 GEM (Wang et al., 2021) served as the reference model, providing the structural and metabolic framework for the reconstruction.

2.7. Gene set analysis

Reporter subsystem and reporter metabolite analyses were performed using the GSAM package (https://github.com/JonathanRob/GeneSetAnalysisMatlab). Differential expression results from 6-month-old APP/PS1 and WT astrocytes, along with gene sets derived from the astrocyte-specific GEM, were used as input. Subsystem and metabolite gene sets were defined by genes encoding reactions within each subsystem or associated with each metabolite. Significance was evaluated using non-directional and distinct-directional p-values, with definitions following the Piano package (Väremo et al., 2013).

2.8. Protein extraction and mass-spectrometry

Proteins were extracted and digested from astrocytes of male 6-month-old APP/PS1 and WT mice ($n = 3$ per group) using the iST kit (PreOmics). Peptides were analyzed by LC-MS on a QE mass spectrometer (Thermo) with a 25 cm C18 column (Ionopticks), using a standard solvent gradient. Data were processed with MaxQuant using the Andromeda search engine against the reviewed mouse Uniprot database, allowing two missed trypsin cleavages, with carbamidomethylation (C) as a fixed and oxidation (M) as a variable modification. FDR was set to 1 %.

2.9. Proteomics analysis

Proteins with missing values in more than half of the total samples (i.e., >3 out of 6) were filtered out prior to analysis. The limma (Ritchie et al., 2015) package was used for normalization and differential expression analysis between the WT and AD groups, setting a threshold of $p < 0.05$ and an absolute $\log_2$FC greater than 0.3 to identify differentially expressed proteins (DEPs).

2.10. Sample preparation for matrix-assisted laser desorption/ionization mass spectrometry imaging (MALDI-MSI)

For 6-month-old male APP/PS1 and WT mice ($n = 3$ per group) anesthetized and killed by cervical dislocation. 10 % carboxymethyl cellulose (Sigma) was used to embed brain tissue in the cassettes.

Tissues were stored at −80 °C and sectioned at 20 μm using a Leica CM1950 cryostat (Leica Microsystems). Sections were mounted on ITO-coated slides (Bruker) for MALDI-MSI or collected for immunofluorescence. Slides were dried in a desiccator (30 min), vacuum-sealed, and stored at −80 °C. A 9-AA matrix in 70 % ethanol was applied using a TM-Sprayer (HTX Technologies) with the following parameters: nozzle velocity 1200 mm/min, track spacing 3 mm, flow rate 0.12 mL/min, spray temperature 90 °C, and nitrogen pressure 10 psi.

2.11. Mass spectrometry imaging

Metabolites in the samples were imaged using a timsTOF fleX MALDI 2 (Bruker) equipped with a 10 kHz smartbeam 3D laser. MALDI2 MSI was operated in positive ion mode in full scan mode for m/z 100–1200. MALDI2 MSI was performed at 20 μm spatial resolution. The frequency of the laser was set to 10,000 Hz, with 60 % the laser energy and 400 laser shots per pixel.

2.12. MALDI-MSI data analysis

Raw imaging data were processed using SCiLS™ Lab 2021 (Bruker Daltonics). A SeuratObject was subsequently constructed utilizing the Seurat (Hao et al., 2021) package. Data normalization employed a dual strategy involving both 9-AA reference compound normalization and total ion count (TIC) normalization. To correct for batch effects in the analysis, we applied the ComBat method from the sva (Leek et al., 2012) package.

This dataset was further used for uniform manifold approximation and projection (UMAP) analyses (McInnes et al., 2020). UMAP reduction results (cell.embeddings) were then used as input data for k-means clustering, specifying the number of clusters (centers) as five and visualized using ggplot2 (Wickham, 2016) package. Adjusted to four clusters to better reflect underlying patterns.

Regions of interest (ROIs) were designated by identifying areas with accumulations of reactive astrocytes in the immunofluorescence-stained sections from MALDI-MSI analysis and their adjacent sections. Using a QuPath to SCiLS™ Lab software plugin in QuPath (Bankhead et al., 2017), the delineated ROI files were then transferred into SCiLS™ Lab.

The differential abundance of metabolites were analyzed using FindMarkers function in Seurat (Hao et al., 2021) (since the values contained negative numbers after batch effect correction, the normalized data was used via the scale data method), with the criteria of an absolute $\log_2$FC greater than 1 and adjusted $p < 0.05$.

2.13. Western blot

Brain tissues from 6-month-old WT mice ($n = 3$) were lysed in RIPA buffer supplemented with protease and phosphatase inhibitors, and homogenized on ice. Proteins were probed with primary antibodies against Perilipin-2 (1:500, Novus) and GAPDH (1:1000, CST), followed by HRP-conjugated secondary antibodies (1:10,000, Jackson ImmunoResearch).

2.14. Single-nucleus RNA sequencing (snRNA-seq) analysis

The snRNA-seq data utilized in this study were sourced from the Allen Institute for Brain Science and are available through the Seattle Alzheimer's Disease Brain Cell Atlas (SEA-AD) (Gabitto et al., 2024) database (https://registry.opendata.aws/allen-sea-ad-atlas). The database contains sequencing samples from the temporal neocortex of 84

donors, who were elderly with ages at death ranging from a minimum of 65 to an average of 88 years. For this study, data on astrocytes were obtained from 6 donors in the Thal 2 Aβ-deposition phase and 9 donors in the Thal 0 Aβ-deposition phase. All selected donors had no clinical diagnosis of dementia. This selection corresponds to 6-month-old AD mice, which have not yet developed dementia and are generally in the stage of normal cognition or mild cognitive impairment. Moreover, among the Aβ-deposition phases, Thal 2 exhibits plaque deposition patterns most similar to those observed in 6-month-old APP/PS1 mice (Whitesell et al., 2018).

For data preprocessing, the downloaded counts table and metadata were used to construct a SeuratObject utilizing the Seurat (Hao et al., 2021) package. Quality control was then applied with criteria specifying that each cell must have more than 2000 but fewer than 7500 RNA sequencing features, and mitochondrial gene content less than 4 %. Data normalization was carried out using the LogNormalize method with a scaling factor set at 10,000. Principal component analysis (PCA) was performed based on the top 2000 most variable genes, followed by UMAP analysis using the top 30 principal components. Clustering was executed at a resolution of 0.5. The cell type markers for the middle temporal gyrus were obtained from CellMarker 2.0 (Hu et al., 2023).

For the single-cell metabolic pathway analysis, the SCPA (Bibby et al., 2022) R package was utilized, offering a novel graph-based test to define pathway activity. Normalized data were derived from astrocytes with Thal 0 and Thal 2. A comprehensive set of 243 metabolic pathways was compiled from the Hallmark (Liberzon et al., 2015), KEGG (Kanehisa et al., 2023), and Reactome (Fabregat et al., 2017) databases. Pathway comparisons were executed using the compare_pathways function in SCPA, setting downsample 4000 to manage data volume. The fatty acid pathway module score was calculated using the AddModuleScore function in Seurat (Hao et al., 2021), based on 158 genes from the Hallmark fatty acid metabolism pathway. The PPAR signaling pathway was modified from Pathview (W and Pathview, 2013) R package.

2.15. Analysis of dietary fatty acids and cognitive function

Data from NHANES (2011–2014, $n = 2{,}502$, age ≥ 60 years) were analyzed to investigate associations between dietary fatty acid intake (SFA, MUFA, PUFA) and cognitive function, assessed by CERAD Word Learning (memory), Animal Fluency (executive function), and Digit Symbol Substitution Test (processing speed and attention) (Centers for Disease Control and Prevention (CDC) and National Center for Health Statistics (NCHS)). Total estimated dietary SFA, MUFA, and PUFA intake (grams, gm), was averaged over the two recall periods (if only the first day was available, that value was used instead of an average). Additionally, participants' intake from dietary supplements during the same periods was considered, with average intakes over the two days calculated when data was available. Total intake of SFA, MUFA, and PUFA was then derived by summing dietary and supplemental sources. Finally, the proportion of each type of fatty acid relative to the total fatty acids was calculated and labeled accordingly as SFAT (Total saturated fatty acids), MFAT (Total monounsaturated fatty acids), and PFAT (Total polyunsaturated fatty acids). Analyses using the survey (Lumley, 2004) R package. The Kruskal-Wallis test was first used to explore the relationship between quartile-based categories of fatty acid intake and cognitive function scores across four tests. Subsequently, linear regression models were employed to examine the relationships between fatty acid intake proportions and cognitive measures. Fatty acid intake was considered both as quartiles and as a continuous variable in the analysis.

2.16. Statistical analysis

For each computational analysis undertaken using previously published codes or resources, the statistical methodologies were adopted as specified in the respective publications and detailed in the corresponding sections of the methods. In vitro experiments involved statistical comparisons across multiple experimental groups using one-way analysis of variance (ANOVA) complemented by Dunnett's multiple comparison test, while the two groups' comparisons were handled through unpaired t-tests.

2.17. Data and code availability

The proteomics data generated in this study have been deposited in iProX (IPX0009463000) and are publicly available. The spot and spectra data related to MALDI-MSI have been deposited in Figshare (https://doi.org/10.6084/m9.figshare.26778319.v1) and are publicly available. All original code has been deposited in GitHub (https://github.com/Jie-Z-159/AD-astrocytes-multiomics.git) and is publicly available.

3. Results

3.1. Astrocytes undergo metabolic changes prior to the onset of AD symptoms

To capture the dynamic transcriptomic changes in astrocytes during AD progression, we re-analyzed RNA-seq data previously published by our laboratory (Pan et al., 2020), which involved astrocytes from 2-, 4-, 6-, 9-, and 12-month-old hemizygous APP/PS1 mice and their WT littermates (Fig. 1A). Our immunofluorescence staining of Aβ (Additional file: Fig. S1) confirmed Aβ plaque distribution across five time points in this AD mouse model. These selected time points span the entire pathological progression in the AD model, providing a foundation for dynamic observational analysis of astrocyte profiles.

In the analysis of differentially expressed genes (DEGs) across various time points, we found that no single gene was consistently upregulated or downregulated throughout the entire series (Additional file: Fig. S2, Fig. S3A). This observation may reflect the complex and dynamic nature of AD progression, where different sets of genes are affected at different stages. Traditional pairwise DEG comparisons are limited to two-group analyses and lack an overall view of multi-time-point data. To address this, we employed singular value decomposition (SVD), a powerful dimensionality reduction technique that decomposes high-dimensional time-series data into dominant temporal expression patterns. Our analysis indicated that the first singular value (519.44) greatly exceeds the others (Fig. 1B), suggesting that its associated pattern represents a consensus transcriptional dynamic shared by most genes. We termed the temporal pattern corresponding to the first singular value as mode 1. This mode captures the majority of gene expression variance across samples. The expression profile of mode 1 showed a significant difference in astrocytes from 6-month-old APP/PS1 mice compared with WT controls (*t*-test, $p = 0.002$, Fig. 1C).

While SVD effectively isolated the primary pattern of gene expression, it did not show the specific genes contributing to this pattern. To bridge this gap, we applied Short Time-series Expression Miner (STEM), which clusters genes with similar temporal dynamics and helps the identification of gene sets aligned with the SVD-derived mode 1. We calculated $\log_2$(AD/WT) expression ratios at each time point, which were then used as input for STEM to extract gene expression profiles. The results showed that profile 5, 10, and 16 were statistically significant. Since the SVD analysis indicated changes around 6 months, we further focused on profiles 16 and 5 (Fig. 1D). GO-BP analysis indicated that genes within profile 16 are predominantly associated with signal transduction and gene expression regulation (Fig. 1E), while profile 5 is associated with organic acid metabolic processes (Fig. 1F). We overlapped the genes in profile 5 with the downregulated DEGs at 6 months, identifying 244 shared genes (Fig. 1G and H). These genes exhibit both disease- and time-dependent downregulation. KEGG pathway analysis of these 244 genes identified 5 enriched pathways, 4 of which were directly associated with fatty acid metabolism. These included the PPAR signaling pathway, biosynthesis of unsaturated fatty acids, fatty acid elongation, and fatty acid metabolism (Fig. 1I). Similarly, we intersected

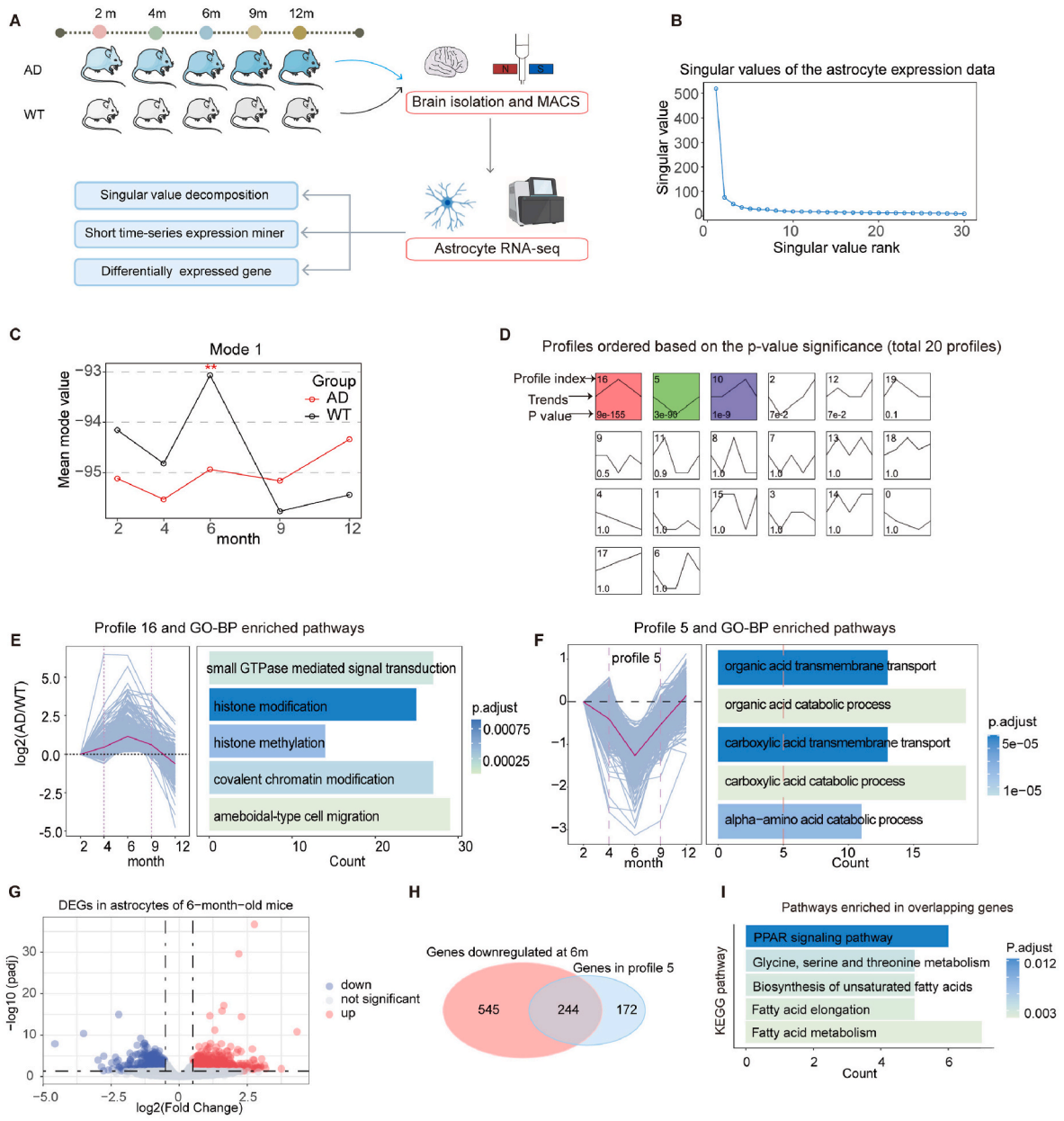

Fig. 1. Astrocytes undergo significant changes in fatty acid metabolism prior to the onset of AD symptoms

A Workflow for the analysis of transcriptomic data across five time points between APP/PS1 and WT astrocytes.

B Singular values of the transcriptomic data matrix after SVD, showing the 30 singular values sorted from largest to smallest.

C Mode 1 expression pattern showing the mean mode value for AD and WT groups across the same age points, t-tests performed between groups at each time point (**$p < 0.01$).

D Twenty predefined profiles from STEM analysis. The number in the top left corner of each profile box is the profile ID. Curves represent expression trends, with the number in the bottom left indicating the p-value. Colored profiles represent statistically significant gene assignments.

E On the left, gray lines represent the expression changes of 583 genes in Profile 16, with the red line indicating the mean expression change. On the right, the top five GO-BP enriched pathways for Profile 16 genes are shown.

F On the left, gray lines represent the expression changes of 416 genes in Profile 5, with the red line indicating the mean expression change. On the right, the top five GO-BP enriched pathways for Profile 5 genes are shown.

G DEGs between APP/PS1 and WT astrocytes at 6 months. The volcano plot displays the log2 fold change in expression (x-axis) and the -log10 adjusted p-values (y-axis). Red dots indicate significantly upregulated genes, blue dots indicate significantly downregulated genes, and gray dots indicate non-significant changes.

IH Venn diagram showing the intersection of significantly downregulated genes at 6 months and genes in Profile 5.I KEGG pathway analysis of intersecting genes, displaying pathways with adjusted p-values less than 0.05.

the genes in profile 16 with the upregulated DEGs at 6 months, resulting in 146 overlapping genes (Additional file: Fig. S3E). However, no pathway was enriched in these genes. Additionally, we selected the top 6 genes from these 244 for validation using qPCR (Additional file: Fig. S3B–C).

3.2. *Astrocyte-specific GEM shows disruptions in fatty acid metabolism*

To further characterize metabolic changes in astrocytes during early progression of AD mouse model, we next integrated the transcriptomic datasets in astrocytes with a mouse genome-scale metabolic model

(GEM) (Wang et al., 2021) (Fig. 2A). GEMs comprise a comprehensive set of mass-balanced metabolic reactions, which are interconnected through shared metabolites to form a complex network. Each reaction is localized to a specific cellular compartment and associated to genes known to code for proteins involved in that reaction. These models offer a powerful framework to gain further biological and mechanistic understanding of metabolism-related diseases, facilitating the identification of potential biomarkers and novel therapeutic targets (Väremo et al., 2015). The astrocyte-specific GEM consists of 7569 reactions, 5851 metabolites, and 1868 genes (Fig. 2B). The majority of the genes included in our astrocyte-specific GEM are actively expressed (TPM $\geq$ 1), whereas only 168 out of 1868 genes exhibit low expression (TPM $<$ 1, Fig. 2C). We extracted 2968 metabolite-gene sets (reporter metabolites) and 131 subsystem-gene sets (reporter subsystems) from this model. Subsystems are groups of reactions forming a pathway or sharing a common metabolic function. Each metabolite (subsystem) gene set is defined by the genes encoding the reactions associated with that metabolite (subsystem). Subsequently, we performed gene set analysis using the differential expression data obtained from APP/PS1 and WT astrocytes at 6 months. Significant gene sets can be interpreted as metabolic hotspots, or metabolites around which important transcriptional changes occur. We found that up-regulated reporter metabolites are enriched of signaling molecules (e.g., cGMP, cAMP, Phosphatidylinositol-3,4,5-trisphosphate), while the down-regulated reporter metabolites are predominantly associated with central energy metabolism (e.g., Acetyl-CoA, NADH, NADPH), and fatty acid metabolism (e.g., Tetracosanoyl-CoA, dihomo-gamma-linolenoyl-CoA, fatty acid pool) (Fig. 2D). Correspondingly, the upregulated reporter subsystem is inositol phosphate metabolism (Fig. 2E). The downregulated reporter subsystems are primarily linked to fatty acid metabolism. These include pathways such as fatty acid oxidation, arachidonic acid (ARA) metabolism, omega-3 fatty acid metabolism, propanoate metabolism, and leukotriene metabolism. Additionally, central energy metabolism pathways—such as the tricarboxylic acid cycle and glyoxylate/dicarboxylate metabolism, and glycolysis/gluconeogenesis—are also downregulated.

3.3. *Downregulation of fatty acid metabolism-related proteins in astrocytes at early stages in AD mouse model*

To investigate the protein-level changes in astrocytes at 6 months, we collected astrocytes from 6-month-old APP/PS1 and WT mice for proteomic analysis. Normalized data were subjected to PCA, showing the distribution of APP/PS1 and WT samples in 3D space (Fig. 3A). We then compared proteins between APP/PS1 and WT mice, identifying a total of 584 DEPs, with 395 upregulated and 189 downregulated

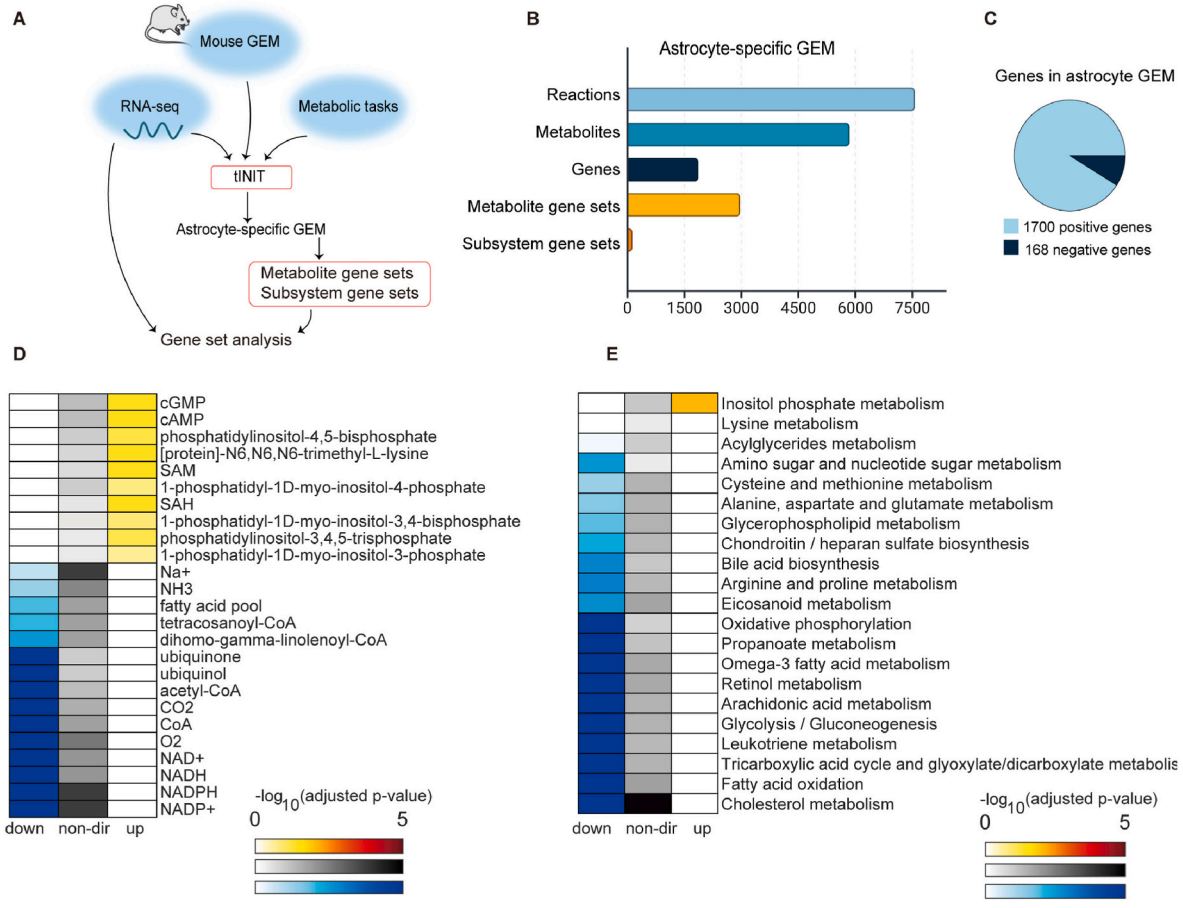

Fig. 2. Astrocyte-specific GEM showed disruptions in fatty acid metabolism-related subsystems and metabolite pathways at early stages of AD mouse model.
A Workflow for the astrocyte-specific GEM construction and analysis.
B The number of reactions, metabolites, genes, and gene set collections included in the astrocyte-specific GEM.
C The composition of positive and negative genes (threshold as 1 TPM) in the astrocyte-specific GEM.
D Top 10 significantly affected reporter metabolite gene sets in APP/PS1 vs. WT astrocytes at 6 months. The non-directional p-values were calculated based on absolute values of the gene p-values without sign information. The up and down p-values were calculated from statistics with sign information.
E Top 10 significantly affected reporter subsystem gene sets in astrocytes from 6-month-old APP/PS1 mice compared with WT controls. The non-directional p-values (non-dir) were calculated based on absolute values of the gene p-values without sign information. The up and down p-values were calculated from statistics with sign information.

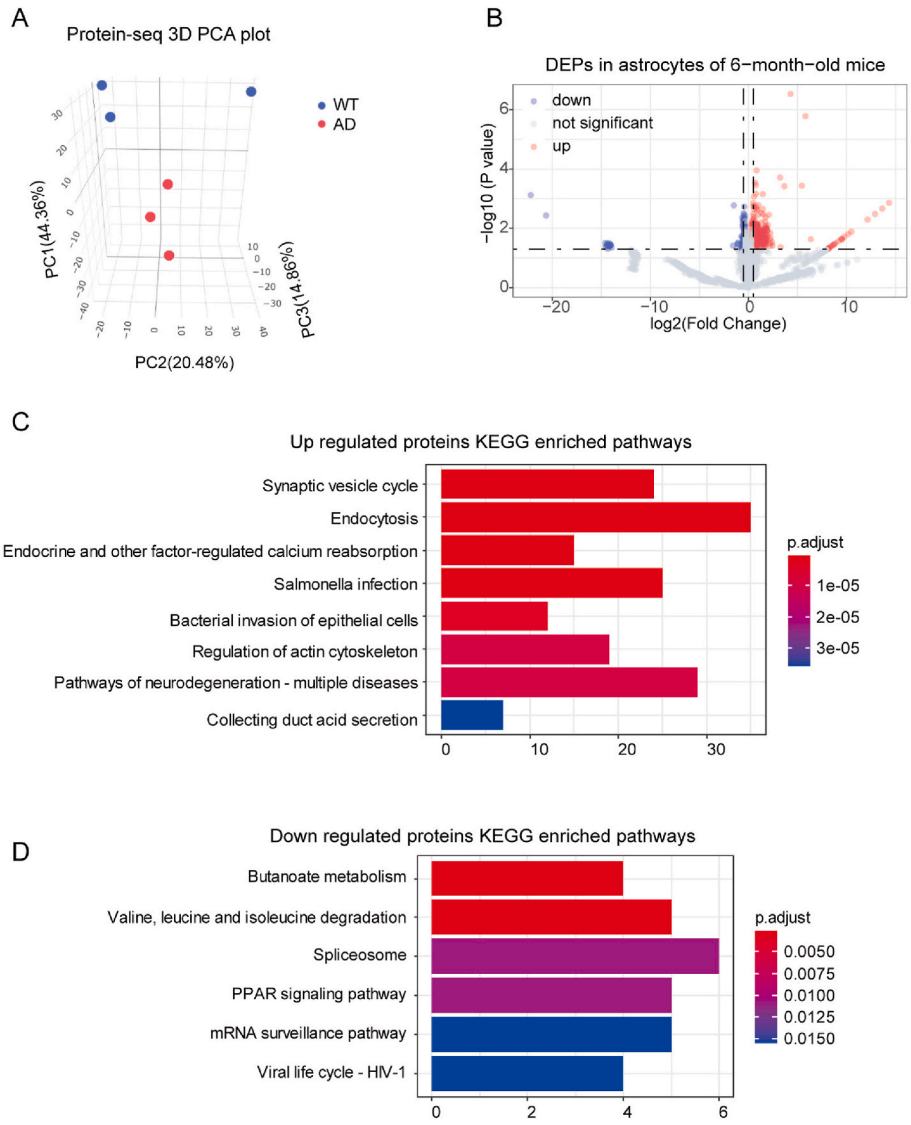

Fig. 3. Downregulation of fatty acid metabolism-related proteins in astrocytes at early stages of AD mouse model
A PCA plot of proteomics data from astrocytes of 6-month-old APP/PS1 and WT mice, showing the first three principal components (PC1-PC3) with the percentage of variance explained by each component indicated in parentheses.
B DEPs in astrocytes of 6-month-old APP/PS1 and WT mice. The volcano plot displays the log2 fold change (x-axis) and -log10 p-value (y-axis). Red dots represent significantly upregulated proteins, blue dots represent significantly downregulated proteins, and gray dots denote non-significant changes.
C KEGG pathway enrichment analysis of upregulated proteins, displaying pathways with adjusted p-values less than 0.05.
D KEGG pathway enrichment analysis of downregulated proteins, displaying pathways with adjusted p-values less than 0.05.

(Fig. 3B). Upregulated proteins were enriched in pathways related to synaptic vesicle cycling, endocytosis, and endocrine-regulated calcium reabsorption (Fig. 3C). In contrast, downregulated proteins were associated with butanoate metabolism, branched-chain amino acid degradation, the spliceosome, and the PPAR signaling pathway (Fig. 3D). Butanoate metabolism and the PPAR signaling pathway are related to fatty acid metabolism. Downregulation of the PPAR signaling pathway was also observed at the RNA level. We also calculated the correlation between transcriptomic and proteomic data for astrocytes at 6 months. Although the correlation is weak (Pearson correlation = 0.11, Fig. S4A), genes differentially regulated at both levels show significant overlap (hypergeometric test $p = 8.32 \times 10^{-9}$ for upregulated genes and $p = 2.06 \times 10^{-8}$ for downregulated genes, Fig. S4E–F). These p-values mean the observed overlap is highly unlikely to have occurred by chance. Among the 23 overlapping downregulated genes, several—including Slc27a1, Fabp7, Slc25a20, and Acsf2—are directly involved in fatty acid uptake, transport, activation, or mitochondrial β-oxidation.

3.4. Spatial insights into metabolic disruptions in early AD mouse model

To further investigate brain metabolite changes, we attempted metabolomic analyses, but the number of sorted astrocytes was insufficient for standard methods. Therefore, we conducted matrix-assisted laser desorption/ionization mass spectrometry imaging (MALDI-MSI) on fresh frozen brain tissue from 6-month-old APP/PS1 and WT mice with a resolution of 20 μm (Fig. 4A). After data preprocessing, and batch effect removal (Methods, Fig. S5A–B), we identified 188 compounds covering various categories such as lipids, carbohydrates, amino acids, and others (Fig. 4B). Firstly, we compared APP/PS1 and WT brain slices, identifying an upregulation of prostaglandin D2−1−glyceryl ester (PGD2-G), phenylacetohydroximoyl−glutathione, 4−CEMA−benzoyl−glutamic acid, and 6−gingesulfonic acid, along with a downregulation of 3−cyclohexyl−1−propylsulfonic acid (Fig. 4C).

Subsequently, we performed k-means clustering on six brain slices, categorizing all spots into four clusters (Fig. 4D and E). Reference to the

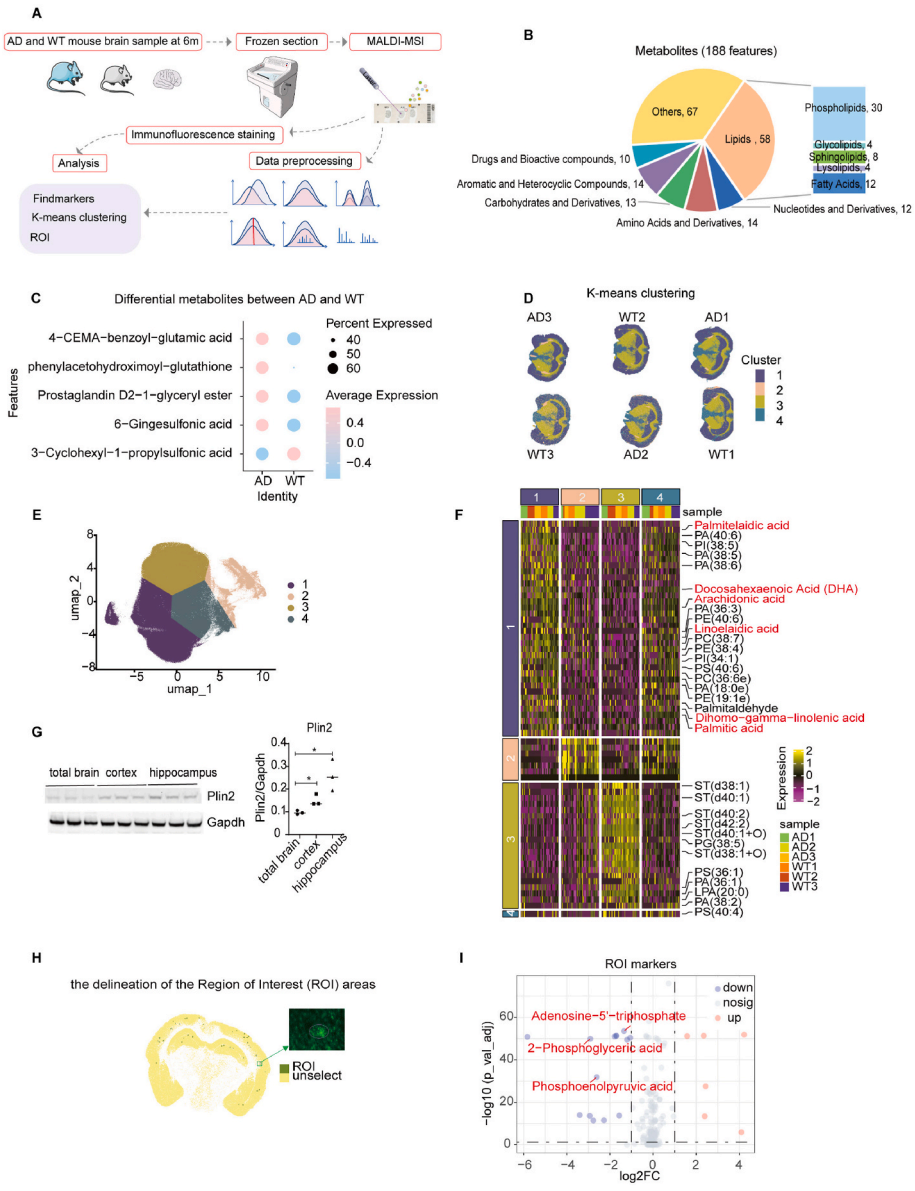

Fig. 4. Spatial insights into metabolic disruptions in early AD mouse model

A Workflow for the analysis of spatial metabolomics data between 6-month-old APP/PS1 and WT brain slices.

B Classification of compounds obtained after data preprocessing.

C Differential metabolites between APP/PS1 and WT brain slices, with dot size indicating expression level and color representing relative changes.

D K-means clustering of all spots into four different clusters, each represented by a specific color.

E UMAP visualization of the four k-means clusters, each represented by a specific color.

F Heatmap of characteristic metabolic markers for each cluster, with fatty acid compounds highlighted in red

G Quantification of plin2 expression levels in whole brain, hippocampus, and cortex using WB, followed by *t*-test analysis, n = 3, $*p < 0.05$.

H Immunofluorescence images using GFAP to delineate regions of reactive astrocyte proliferation, projected onto the spatial metabolomics spots. Green dots represent the region of interest (ROI), while yellow dots represent the remaining control areas within cluster 1. This diagram corresponds to AD1.

I Differential metabolites between the ROIs and the unselected regions of cluster 1. The volcano plot displays the log2 fold change (x-axis) and -log10 adjusted p-values (y-axis). Red dots represent significantly upregulated metabolites, blue dots represent significantly downregulated metabolites, and gray dots denote non-significant changes.

mouse brain atlas (Fig. S5C) shows that the four clusters closely match the anatomical structure of brain. Cluster 1 predominantly covered the hippocampus and cortex; cluster 2 was mainly located in the lateral ventricle or non-tissue areas caused by sectioning; cluster 3 concentrated in the fiber tracts, thalamus, and hypothalamic lateral zone; and cluster 4 involved the periventricular region, hypothalamic medial zone and part of the midbrain. The spatial distribution of metabolites is consistent with structure and function of brain regions (Fig. 4F). For instance, markers of cluster 3 included many sulfatides (ST), which are primarily found in the myelin sheath of the CNS produced by oligodendrocytes. Cluster 1 was significantly enriched with various fatty acids, including palmitelaidic acid, docosahexaenoic acid (DHA), arachidonic acid, dinoelaidic acid, dihomo-gamma-linolenic acid, and palmitic acid (Fig. 4F). To explore whether fatty acids are indeed enriched in the hippocampus and cortex, we examined the expression of Plin2 (a lipid droplet-associated protein that regulates fatty acid storage) in whole brain, hippocampus, and cortex (Fig. 4G).

Due to the lack of specific metabolic markers for astrocytes, we could

not directly assess metabolic changes in individual astrocytes at early AD stages. However, GFAP staining of the MALDI-MSI–analyzed brain slices and their adjacent sections (Additional file: Fig. S5D) revealed regions with reactive astrocyte accumulation, which we defined as regions of interest (ROI, Fig. 4H). Astrocytosis parallels plaque deposition, with severe astrocytosis at 6 months near plaques. Therefore, our defined ROIs closely aligned with the core pathological regions of AD mouse model. Given that GFAP-positive astrocyte aggregates were predominantly localized to Cluster 1 (hippocampus and cortex), comparing GFAP-positive ROIs and negative areas within this cluster helped control for region-specific metabolic variability, thereby allowing a more accurate characterization of astrocyte-associated metabolic changes. Among the differentially abundant metabolites (Additional file: Fig. S6), adenosine-5′-triphosphate (ATP), 2-phosphoglyceric acid,

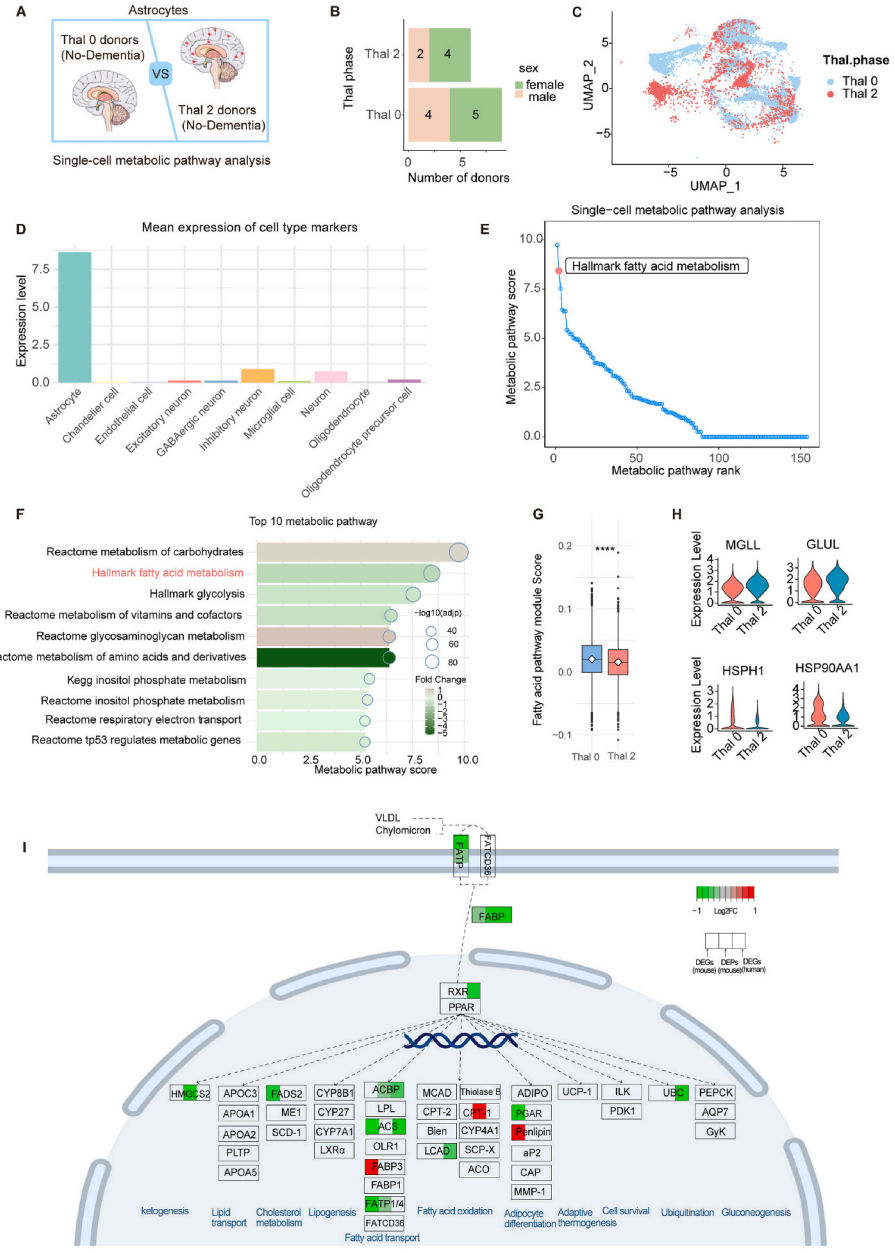

Fig. 5. Human astrocytes have deficiency in fatty acid metabolism in Thal 2 Aβ-deposition phases

A Workflow for single-cell astrocyte analysis from human donors at Thal 0 and Thal 2 Aβ-deposition phase.

B Sex composition of donors included in the study.

C UMAP visualization of preprocessed single-cell astrocyte data, color-coded by Aβ-deposition phases.

D Mean expression levels of different cell type-specific markers.

E Metabolic pathways ranked by SCAP-calculated pathway scores, with the fatty acid metabolism pathway from the Hallmark database highlighted in red.

F Top ten metabolic pathways ranked by SCAP-calculated pathway scores, with blue circles representing adjusted p-values and bar colors indicating log2 fold change values.

G Box plot showing the distribution of fatty acid metabolism module scores between cells from Thal 2 and Thal 0 controls. Wilcoxon's rank-sum test, $^{****}p < 0.001$.

H Violin plots showing the top two upregulated (MGLL, GLUL) and downregulated (HSPH1, HSP90AA1) genes between Thal 0 and Thal 2 phases in the Hallmark fatty acid metabolism pathway.patial insights into metabolic disruptions

I DEGs and DEPs in the PPAR signaling pathway between astrocytes from early Aβ-deposition phases and normal conditions in mouse and human. Node colors represent Log2FC values, with green indicating downregulation and red indicating upregulation.

and phosphoenolpyruvic acid, which are key intermediates of glycolysis, were downregulated in the ROI regions (Fig. 4I).

3.5. Human astrocytes have deficiency in fatty acid metabolism in early AD

To extend our findings from animal models to human, we analyzed single-nucleus RNA sequencing data from the Seattle Alzheimer's Disease Brain Cell Atlas (SEA-AD) dataset (Gabitto et al., 2024) (Fig. 5A). Our analysis focused on astrocytes from 6 donors in the Thal phase 2 of Aβ deposition and 9 donors in the Thal phase 0 (Fig. 5B). None of the selected donors had a clinical diagnosis of dementia. Among Aβ deposition phases, Thal phase 2 most closely resembles the plaque distribution observed in 6-month-old APP/PS1 mice (Whitesell et al., 2018). To confirm the identity of the astrocyte population used in our analysis (Fig. 5C), we evaluated the expression of canonical marker genes and confirmed a clear enrichment of astrocyte markers (Fig. 5D). Next, we applied SCPA (Bibby et al., 2022), a pathway analysis method specifically designed for single-cell data, to identify metabolic pathways that are differentially regulated between astrocytes in the Thal 2 group and the control group (Thal 0). SCPA uses a graph-based non-parametric statistical model to assign a score to each pathway, quantifying the degree of differential gene distribution. We analyzed a total of 243 metabolic pathways obtained from the Hallmark (Liberzon et al., 2015), KEGG (Kanehisa et al., 2023), and Reactome (Fabregat et al., 2017) databases. These pathways were ranked based on their SCPA score, among which "Hallmark fatty acid metabolism" ranked second, highlighting differences in astrocytic fatty acid metabolism between the early pathological stage and no pathology stage (Fig. 5E). Notably, the fatty acid metabolism pathway and glycolysis exhibited negative fold changes in the Thal 2 group (Fig. 5F), consistent with previous findings based on transcriptomics, proteomics, and spatial metabolomics, further suggesting deficiency of energy metabolism in astrocytes during early AD. We assessed the activity of the fatty acid metabolism pathway at the single-cell level by calculating module scores for 157 genes within the Hallmark fatty acid metabolism pathway, using Seurat's AddModuleScore function (Hao et al., 2021). The results showed a reduction in fatty acid metabolism module scores in astrocytes from the Thal 2 group compared to the Thal 0 group at single-cell level (Wilcoxon's rank-sum test, $p = 8 \times 10^{-13}$; Fig. 5G). Within the fatty acid metabolism pathway, the top two upregulated genes were MGLL ($\log_2$FC = 0.54) and GLUL ($\log_2$FC = 0.50), while the top two downregulated genes were HSPH1 ($\log_2$FC = −1.54) and HSP90AA1 ($\log_2$FC = −1.43) (Fig. 5H).

Once exogenous lipid molecules are taken up by cells, fatty acids can be released and combined with glycerol to form triglycerides, which are subsequently sequestered into lipid droplets (LDs) regulated by LD-associated proteins, such as Plin2. During fluctuations in cellular fatty acid levels, Fatty acids binding proteins (FABPs) can regulate the formation and utilization of LDs (Zhang et al., 2024). FABPs facilitate Fatty acids transport to the nucleus. In the nucleus, fatty acids and their derivatives activate PPARs and finally regulates the transcription of genes involved in fatty acid transport, ketogenesis, cholesterol metabolism, and others.

Among FABPs, FABP5 is expressed in neurons and glia, and FABP7 is most abundantly expressed in astrocytes and precursor cells (Owada et al., 1996; Owada, 2008). While FABP7 can bind a range of ligands, it has particularly high affinity for n-3 polyunsaturated fatty acids, such as DHA (Needham et al., 2022). In our mouse data, FABP7 was downregulated at both the transcript ($\log_2$FC = −1.36) and protein levels ($\log_2$FC = −1.13), and FABP5 was downregulated in the human data ($\log_2$FC = −0.97). Consistently, the PPAR signaling pathway was downregulated (Figs. 1I and 3D). Omega-3 fatty acid metabolism was also found to be downregulated in the GEM model (Fig. 2E). These findings point to impaired transport of n-3 polyunsaturated fatty acids and reduced PPAR-mediated transcriptional activity. Given the enrichment of fatty acids in the cortex and hippocampus (Fig. 4F), these brain regions may be particularly vulnerable to such disturbances in early AD. We projected the DEGs and DEPs onto the PPAR signaling pathway (Fig. 5I).

4. Discussion

AD is a neurodegenerative disorder characterized by profound complexity (Seto et al., 2021). Astrocytes remain insufficiently explored regarding their dynamic roles. Although the early, pre-symptomatic stages of AD are increasingly recognized as crucial for understanding disease onset, astrocytes during this phase remain understudied. In this study, we systematically confirm the disruption of fatty acid metabolism in astrocytes during early AD at the RNA, protein, and metabolite levels. Specifically, we identify a coordinated downregulation of FABPs and the PPAR signaling pathway, which may suggest impaired fatty acid trafficking and nuclear lipid signaling.

Astrocytes are the primary cell type responsible for fatty acid metabolism in brain tissue (Fecher et al., 2019) and an important source of polyunsaturated fatty acids (PUFA) such as DHA (an omega-3 fatty acid) and ARA (Aizawa et al., 2016). Interestingly, the relationship between the proportions of different dietary fatty acids and cognitive function (Additional file: Fig. S7A) supported that a higher proportion of saturated fatty acids (SFA) intake has a negative association with cognitive function, while a higher proportion of PUFA intake has a positive association (Additional file: Fig. S7B–C). Consistent with these findings, supplementation with omega-3 fatty acids has shown potential in improving cognitive functions in mild AD patients (Canhada et al., 2018). In line with this pattern, in astrocytes from 6-month-old APP/PS1 mice, omega-3 fatty acid metabolism and ARA metabolism were down-regulated (Fig. 2E). Given the importance of PUFA in maintaining neuronal health, restoring proper fatty acid metabolism in astrocytes may offer a promising strategy for early intervention. In addition, modest pharmacological activation of astrocytic lipid sensing, for example with brain-penetrant PPAR-α/γ agonists, could provide a complementary way to restore fatty acid oxidation and transport. Our study suggests that FABP7/5 are closely involved in astrocytic changes during early AD. To date, research on FABP7/5 has been limited, with most studies focusing on neurodevelopment and cancer. While increased FABP7 expression has been reported in late-stage AD (Hamilton et al., 2024), our data reveal a distinct pattern in astrocytes during early-stage AD, where FABP7/5 is significantly downregulated. This stage- and cell-type-specific difference suggests that FABP7/5 may contribute to astrocyte-mediated fatty acid dysregulation in early AD pathogenesis, and highlights their potential as early molecular indicators or therapeutic targets. Accordingly, pre-clinical approaches that up-regulate FABP5/7 expression or stability may also help restore intracellular fatty acid trafficking.

Relatedly, reactive astrogliosis is a recognized feature of AD and can have context-dependent effects (Rodríguez et al., 2009). Several observations point to a link between astrocytic fatty acid regulation and reactivity. Impaired fatty acid degradation in astrocytes leads to lipid accumulation and is accompanied by STAT3 acetylation–associated reactive astrogliosis (Mi et al., 2023); saturated fatty acids such as palmitate increase GFAP expression (Oliveira et al., 2018); and ~95 % of HADHA, a core FAO enzyme, colocalizes with $GFAP^+$ astrocytes, suggesting that reactive astrocytes may be a major site of FAO (Xiong et al., 2022). In parallel, fatty acids engage inflammatory signaling in astrocytes: DHA can attenuate IL-1β–induced pro-inflammatory responses, whereas saturated long-chain fatty acids promote the release of TNFα and IL-6 (Zgórzyńska et al., 2021; Gupta et al., 2012). Overall, these findings suggest an association between astrocytic fatty acid metabolism and gliosis/inflammation and motivate targeted studies to assess potential cross-effects.

To achieve a comprehensive understanding of the alterations in astrocytic metabolism during AD, there is still room for further exploration. For instance, *in vivo* 13C-Metabolic Flux Analysis (13C-MFA) that

directly measures metabolic fluxes related to fatty acids can be conducted to validate our findings and precisely analyze the metabolic changes within astrocytes in AD. However, 13C-MFA is specifically designed to quantify fluxes within small metabolic networks (typically central carbon metabolism), and its implementation can be both experimentally and computationally costly, especially for *in vivo* systems (Lagziel et al., 2019). Furthermore, the current limitations of spatial metabolomics in metabolite identification and resolution, combined with a lack of information on astrocytic metabolic biomarkers, hindered this study's ability to identify the specific metabolites associated linked to fatty acid metabolism in astrocytes of early AD mouse models. We also note that the lack of consistent DEGs across all time points in our transcriptomic analysis may reflect the complex and dynamic nature of AD progression. However, it could also result from technical limitations such as the relatively small sample size ($n = 3$ per group), inter-animal variability, low expression levels of certain genes, and the statistical methods employed, which may have limited the ability to detect consistent DEGs. Moreover, the animal model used in this experiment, the APP/PS1 mouse, does not simulate tau protein-related neurofibrillary tangles, which is also a limitation of this study. Nevertheless, despite these limitations and the relatively small fold changes, the convergence of results across independent omics layers, including transcriptomics, proteomics, and metabolomics, consistently points in the same direction, offering valuable information about astrocytic fatty acid metabolism during early AD. These findings provide insights that could inform the development of future diagnostic and therapeutic strategies.

CRediT authorship contribution statement

Jie Zhong: Writing – original draft, Methodology, Investigation, Formal analysis, Data curation, Conceptualization. **Manhui Li:** Methodology. **Ziwei Dai:** Writing – review & editing, Supervision, Resources, Methodology, Funding acquisition. **Jun Wan:** Resources, Funding acquisition.

Funding declaration

This work was supported by National Key Research and Development Program of China (2021YFF1201000 to Z.D.), Guangxi Natural Science Foundation (2020GXNSFDA238009 to J.W.), National Natural Science Foundation of China (82071586 to J.W. and 12371489 to Z.D.), Guangdong Innovative and Entrepreneurial Research Team Program (2021ZT09Y104 to J.W.), Guangdong Program (2021QN02Y856 to Z. D.) and Shenzhen Science and Technology Basic Research Program (JCYJ20220818100215033 to J.W.).

Declaration of competing interest

The authors declare that they have no known competing financial interests or personal relationships that could have appeared to influence the work reported in this paper.

Acknowledgments

We are grateful for the support of the Shenzhen - Peking Universityy - the Hong Kong University of Science and Technology Medical Center and Southern University of Science and Technology Platform. In the workflow figures, the brain, mouse, and human icons were modified from Servier Medical Art (http://smart.servier.com/). In Fig. 1A, the RNA-seq icon was adapted from Wikimedia Commons (https://commons.wikimedia.org/wiki/File:RNA-seq.jpg). In Fig. 4A, the cryostat icon was adapted from Wikimedia Commons (https://commons.wikimedia.org/wiki/File:201804_Cryostat.svg). All icons are used under the terms of the Creative Commons Attribution 4.0 Generic License (https://creativecommons.org/licenses/by/4.0/).

Appendix A. Supplementary data

Supplementary data to this article can be found online at https://doi.org/10.1016/j.neuint.2025.106049.

Data availability

The link to data and code has been included in the "Data and code availability" subsection of the Methods.

References

Agren, R., et al., 2014. Identification of anticancer drugs for hepatocellular carcinoma through personalized genome-scale metabolic modeling. Mol. Syst. Biol. 10, 721.
Aizawa, F., et al., 2016. Astrocytes release polyunsaturated fatty acids by lipopolysaccharide stimuli. Biol. Pharm. Bull. 39, 1100–1106.
Baldwin, K.T., Murai, K.K., Khakh, B.S., 2024. Astrocyte morphology. Trends Cell Biol. 34, 547–565.
Bankhead, P., et al., 2017. QuPath: open source software for digital pathology image analysis. Sci. Rep. 7, 16878.
Bellaver, B., et al., 2023. Astrocyte reactivity influences amyloid-β effects on tau pathology in preclinical Alzheimer's disease. Nat. Med. 29, 1775–1781.
Bibby, J.A., et al., 2022. Systematic single-cell pathway analysis to characterize early T cell activation. Cell Rep. 41, 111697.
Canhada, S., Castro, K., Perry, I.S., Luft, V.C., 2018. Omega-3 fatty acids' supplementation in Alzheimer's disease: a systematic review. Nutr. Neurosci. 21, 529–538.
Centers for Disease Control and Prevention (CDC). National Center for Health Statistics (NCHS). National health and nutrition examination survey data. Hyattsville, MD: U. S. Department of Health and Human Services, Centers for Disease Control and Prevention [2011-2014]. https://www.cdc.gov/nchs/nhanes/index.htm.
Chen, H., Boutros, P.C., 2011. VennDiagram: a package for the generation of highly-customizable venn and euler diagrams in R. BMC Bioinf. 12, 35.
Chun, H., Lee, C.J., 2018. Reactive astrocytes in Alzheimer's disease: a double-edged sword. Neurosci. Res. 126, 44–52.
Drew, L., 2018. An age-old story of dementia. Nature 559, S2–S3.
Ernst, J., Bar-Joseph, Z., 2006. STEM: a tool for the analysis of short time series gene expression data. BMC Bioinf. 7, 191.
Fabregat, A., et al., 2017. Reactome pathway analysis: a high-performance in-memory approach. BMC Bioinf. 18, 142.
Fecher, C., et al., 2019. Cell-type-specific profiling of brain mitochondria reveals functional and molecular diversity. Nat. Neurosci. 22, 1731–1742.
Gabitto, M.I., et al., 2024. Integrated multimodal cell atlas of Alzheimer's disease. Nat. Neurosci. 27, 2366–2383.
Garcia-Alloza, M., et al., 2006. Characterization of amyloid deposition in the APPswe/PS1dE9 mouse model of alzheimer disease. Neurobiol. Dis. 24, 516–524.
Gupta, S., Knight, A.G., Gupta, S., Keller, J.N., Bruce-Keller, A.J., 2012. Saturated long chain fatty acids activate inflammatory signaling in astrocytes. J. Neurochem. 120, 1060–1071.
Hamilton, H.L., et al., 2024. FABP7 drives an inflammatory response in human astrocytes and is upregulated in Alzheimer's disease. GeroScience 46, 1607–1625.
Hao, Y., et al., 2021. Integrated analysis of multimodal single-cell data. Cell 184, 3573–3587.e29.
Hu, C., et al., 2023. CellMarker 2.0: an updated database of manually curated cell markers in human/mouse and web tools based on scRNA-seq data. Nucleic Acids Res. 51, D870–D876.
Jack, C.R., et al., 2010. Hypothetical model of dynamic biomarkers of the Alzheimer's pathological Cascade. Lancet Neurol. 9, 119–128.
Jack, C.R., et al., 2013. Tracking pathophysiological processes in Alzheimer's disease: an updated hypothetical model of dynamic biomarkers. Lancet Neurol. 12, 207–216.
Janus, C., Flores, A.Y., Xu, G., Borchelt, D.R., 2015. Behavioral abnormalities in APPSwe/PS1dE9 mouse model of AD-like pathology: comparative analysis across multiple behavioral domains. Neurobiol. Aging 36, 2519–2532.
Kanehisa, M., Furumichi, M., Sato, Y., Kawashima, M., Ishiguro-Watanabe, M., 2023. KEGG for taxonomy-based analysis of pathways and genomes. Nucleic Acids Res. 51, D587–D592.
Lagziel, S., Lee, W.D., Shlomi, T., 2019. Studying metabolic flux adaptations in cancer through integrated experimental-computational approaches. BMC Biol. 17, 51.
Lalonde, R., Kim, H.D., Maxwell, J.A., Fukuchi, K., 2005. Exploratory activity and spatial learning in 12-month-old APP(695)SWE/co+PS1/DeltaE9 mice with amyloid plaques. Neurosci. Lett. 390, 87–92.
Lee, H.-G., Lee, J.-H., Flausino, L.E., Quintana, F. J. Neuroinflammation, 2023. An astrocyte perspective. Sci. Transl. Med. 15, eadi7828.
Leek, J.T., Johnson, W.E., Parker, H.S., Jaffe, A.E., Storey, J.D., 2012. The sva package for removing batch effects and other unwanted variation in high-throughput experiments. Bioinforma. Oxf. Engl. 28, 882–883.
Liberzon, A., et al., 2015. The molecular signatures database (MSigDB) hallmark gene set collection. Cell Syst. 1, 417–425.
Love, M.I., Huber, W., Anders, S., 2014. Moderated estimation of fold change and dispersion for RNA-Seq data with DESeq2. Genome Biol. 15, 550.
Lumley, T., 2004. Analysis of complex survey samples. J. Stat. Software 9, 1–19.

Ma, N., et al., 2019. Whole-transcriptome analysis of APP/PS1 mouse brain and identification of circRNA-miRNA-mRNA networks to investigate AD pathogenesis. Mol. Ther. Nucleic Acids 18, 1049–1062.
Mahaman, Y.A.R., et al., 2022. Biomarkers used in Alzheimer's disease diagnosis, treatment, and prevention. Ageing Res. Rev. 74, 101544.
Mathys, H., et al., 2019. Single-cell transcriptomic analysis of Alzheimer's disease. Nature 570, 332–337.
McInnes, L., Healy, J., Melville, J.U.M.A.P., 2020. Uniform manifold approximation and projection for dimension reduction. Preprint at. https://doi.org/10.48550/arXiv.1802.03426.
Mi, Y., et al., 2023. Loss of fatty acid degradation by astrocytic mitochondria triggers neuroinflammation and neurodegeneration. Nat. Metab. 5, 445–465.
Murdock, M.H., 2023. Insights into Alzheimer's disease from single-cell genomic approaches. Nat. Neurosci. 26.
Nam, M.-H., et al., 2023. Visualizing reactive astrocyte-neuron interaction in Alzheimer's disease using 11C-acetate and 18F-FDG. Brain J. Neurol. 146, 2957–2974.
Needham, H., et al., 2022. A dichotomous role for FABP7 in sleep and alzheimer's disease pathogenesis: a hypothesis. Front. Neurosci. 16.
Oliveira, A., de, A.B., et al., 2018. Palmitate treated-astrocyte conditioned medium contains increased glutathione and interferes in hypothalamic synaptic network in vitro. Neurochem. Int. 120, 140–148.
Owada, Y., 2008. Fatty acid binding protein: localization and functional significance in the brain. Tohoku J. Exp. Med. 214, 213–220.
Owada, Y., Yoshimoto, T., Kondo, H., 1996. Spatio-temporally differential expression of genes for three members of fatty acid binding proteins in developing and mature rat brains. J. Chem. Neuroanat. 12, 113–122.
Pan, J., Ma, N., Yu, B., Zhang, W., Wan, J., 2020. Transcriptomic profiling of microglia and astrocytes throughout aging. J. Neuroinflammation 17, 97.
Park, M.W., et al., 2021. NOX4 promotes ferroptosis of astrocytes by oxidative stress-induced lipid peroxidation via the impairment of mitochondrial metabolism in Alzheimer's diseases. Redox Biol. 41, 101947.
Pathak, C., Kabra, U.D., 2024. A comprehensive review of multi-target directed ligands in the treatment of Alzheimer's disease. Bioorganic Chem.
Richard, B.C., et al., 2015. Gene dosage dependent aggravation of the neurological phenotype in the 5XFAD mouse model of alzheimer's disease. J. Alzheim. Dis. 45, 1223–1236.
Ritchie, M.E., et al., 2015. Limma powers differential expression analyses for RNA-Sequencing and microarray studies. Nucleic Acids Res. 43 e47–e47.
Rodríguez, J.J., Olabarria, M., Chvatal, A., Verkhratsky, A., 2009. Astroglia in dementia and Alzheimer's disease. Cell Death Differ. 16, 378–385.
Sekar, S., et al., 2015. Alzheimer's disease is associated with altered expression of genes involved in immune response and mitochondrial processes in astrocytes. Neurobiol. Aging 36, 583–591.
Seto, M., Weiner, R.L., Dumitrescu, L., Hohman, T.J., 2021. Protective genes and pathways in Alzheimer's disease: moving towards precision interventions. Mol. Neurodegener. 16, 29.
Shannon, P., et al., 2003. Cytoscape: a software environment for integrated models of biomolecular interaction networks. Genome Res. 13, 2498–2504.
Sims, J.R., et al., 2023. Donanemab in early symptomatic alzheimer disease: the TRAILBLAZER-ALZ 2 randomized clinical trial. JAMA 330, 512–527.
The Singular Value Decomposition (SVD), 2002. Fundamentals of Matrix Computations, vols. 261–288. https://doi.org/10.1002/0471249718.ch4.
Thomas, P.D., et al., 2022. PANTHER: making genome-scale phylogenetics accessible to all. Protein Sci. 31, 8–22.
Uddin, M.S., Lim, L.W., 2022. Glial cells in Alzheimer's disease: from neuropathological changes to therapeutic implications. Ageing Res. Rev. 78, 101622.
van Dyck, C.H., et al., 2023. Lecanemab in early alzheimer's disease. N. Engl. J. Med. 388, 9–21.
Väremo, L., Nielsen, J., Nookaew, I., 2013. Enriching the gene set analysis of genome-wide data by incorporating directionality of gene expression and combining statistical hypotheses and methods. Nucleic Acids Res. 41, 4378–4391.
Väremo, L., et al., 2015. Proteome- and transcriptome-driven reconstruction of the human myocyte metabolic network and its use for identification of markers for diabetes. Cell Rep. 11, 921–933.
Verkhratsky, A., Nedergaard, M., 2018. Physiology of astroglia. Physiol. Rev. 98, 239–389.
Verkhratsky, A., Olabarria, M., Noristani, H.N., Yeh, C.-Y., Rodriguez, J.J., 2010. Astrocytes in Alzheimer's disease. Neurotherapeutics 7, 399–412.
Verkhratsky, A., Rodrigues, J.J., Pivoriunas, A., Zorec, R., Semyanov, A., 2019. Astroglial atrophy in Alzheimer's disease. Pflügers Archiv 471, 1247–1261.
Volianskis, A., Køstner, R., Mølgaard, M., Hass, S., Jensen, M.S., 2010. Episodic memory deficits are not related to altered glutamatergic synaptic transmission and plasticity in the CA1 hippocampus of the APPswe/PS1δE9-deleted transgenic mice model of ß-amyloidosis. Neurobiol. Aging 31, 1173–1187.
W, L., Pathview, C.B., 2013. An R/Bioconductor package for pathway-based data integration and visualization. Bioinforma. Oxf. Engl. 29.
Wang, H., et al., 2021. Genome-scale metabolic network reconstruction of model animals as a platform for translational research. Proc. Natl. Acad. Sci. 118, e2102344118.
Wang, G., et al., 2022. Spatial dynamic metabolomics identifies metabolic cell fate trajectories in human kidney differentiation. Cell Stem Cell 29, 1580–1593.e7.
Whitesell, J.D., et al., 2018. Whole brain imaging reveals distinct spatial patterns of amyloid beta deposition in three mouse models of Alzheimer's disease. J. Comp. Neurol. 527, 2122.
Wickham, H., 2016. Ggplot2. Springer International Publishing, Cham. https://doi.org/10.1007/978-3-319-24277-4.
Xiong, X.-Y., Tang, Y., Yang, Q.-W., 2022. Metabolic changes favor the activity and heterogeneity of reactive astrocytes. Trends Endocrinol. Metabol. 33, 390–400.
Yeh, C.-Y., Vadhwana, B., Verkhratsky, A., Rodríguez, J.J., 2011. Early astrocytic atrophy in the entorhinal cortex of a triple transgenic animal model of alzheimer's disease. ASN Neuro 3, AN20110025.
Yu, G., Wang, L.-G., Han, Y., He, Q.-Y., 2012. clusterProfiler: an R package for comparing biological themes among gene clusters. OMICS A J. Integr. Biol. 16, 284–287.
Zgórzyńska, E., Stulczewski, D., Dziedzic, B., Su, K.-P., Walczewska, A., 2021. Docosahexaenoic fatty acid reduces the pro-inflammatory response induced by IL-1β in astrocytes through inhibition of NF-κB and AP-1 transcription factor activation. BMC Neurosci. 22, 4.
Zhang, X., Chen, C., Liu, Y., 2024. Navigating the metabolic maze: anomalies in fatty acid and cholesterol processes in Alzheimer's astrocytes. Alzheimers Res. Ther. 16, 63.